REVIEW ARTICLE

Recent Developments in Geotechnique for Earthquake Engineering

Arsalan Ghahramani[1]

This paper presents an overview of important recent developments in geotechnique for earthquake engineering. Major earthquakes have made possible the validation and improvement of soil subjected to liquefaction by field performance of standard penetration test, cone penetration test and shear wave velocity measurements. Site effects, earth pressure on retaining walls, as well as, seismic bearing capacity factors for clayey and sandy soils have become more explicable with the use of these new results.

INTRODUCTION

Major contributions in analysis of geotechnical characteristics leading to a more fundamental understanding have been made through the study of some recent catastrophic earthquakes. These improvements especially pertain to liquefaction, site effects and damage. There has been theoretical advancements concerning evaluation of dynamic earth pressure and seismic bearing capacity factors. Some of the major earthquakes, which their analyses have assisted in these recent developments, are listed below:

1. Loma Prieta, October 17, 1989, California, USA, M = 7.1.
2. Roodbar-Manjil, June 20, 1990, Iran, M = 7.3.
3. Northern Luzon, July 16, 1990, Philippines, M = 7.7.
4. Costa Rica, April 22, 1991, M = 7.5.
5. Erzincan, March 13, 1991, M = 6.5.
6. Northridge, January 17, 1994, California, USA, M = 6.7.
7. Kobe, January 16, 1995, Japan, M = 7.2.

Although these earthquakes provide great impetus for engineering researches, they also cause unprecedented human lost (30,000 in Roodbar-Manjil, Iran) and enormous damages to properties (15 billion dollars in Northridge, between 80 and 100 billion dollars in Kobe). The study of liquefaction including the site performance prediction of standard penetration test, cone penetration and shear wave velocity has been improved. The evaluation of piezocone testing, pattern recognition techniques and the spectral analysis of surface waves are recent developments in liquefaction prediction for earthquake engineering.

Numerous acceleration records made available by these major earthquakes have had considerable impact on evaluation of site effects and this may lead to amendment, to the common codes for earthquake design.

1. Shiraz University, Shiraz, I.R. Iran and visiting professor, University of Canterbury, Christchurch, New Zealand.

Scientia Iranica, Vol. 2, No. 2, © Sharif University of Technology, July 1995.

Evaluation and analysis of life line damage have resulted in new developments for damage rate and appraisal, especially in the case of water and gas lines.

Furthermore, on the theoretical side, recent improvements include calculation of the dynamic active earth pressure coefficients and seismic bearing capacity factors for clayey and sandy soils.

LIQUEFACTION

Epicentral Distance

The maximum epicentral distance to liquefied sites, as a function of magnitude, has been studied by Yoshida [1] and Wakamatsu [2] as presented in Figures 1, 2 and 3. These figures show that for major earthquakes, distance of up to 200 km can be effected by liquefaction, thus, the liquefaction damage is much more extensive than damages for earthquakes on normal grounds.

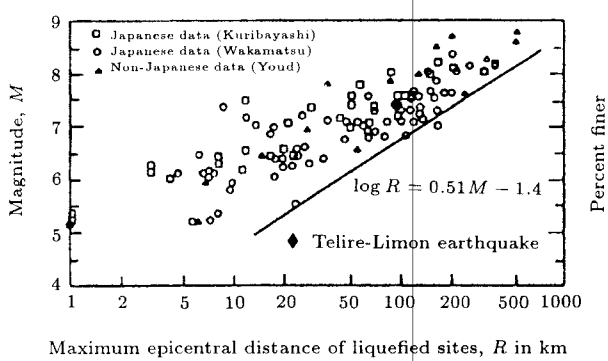

Figure 1. Maximum epicentral distance to liquefied site versus magnitude relationships. Reprinted from Yoshida [1], National Center for Earthquake Engineering Recearch (NCEER).

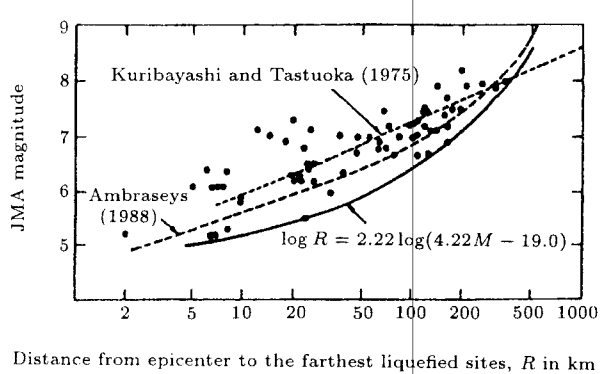

Figure 2. Epicentral Distance to the farthest liquefied sites, for 67 earthquakes after 1884. Reprinted from Wakamatsu [2], NCEER.

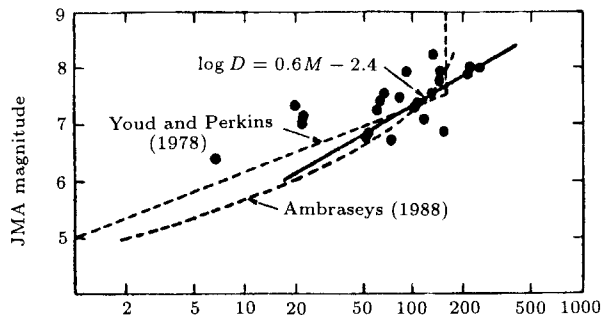

Figure 3. Source distance to the farthest liquefied sites, for 23 earthquakes after 1884. Reprinted from Wakamatsu [2], NCEER.

Liquefaction Measurement During an Earthquake

The actual soil behavior of liquefaction during an earthquake is recorded by Elgamal [3]. The site profile and instrumentation are shown in Figure 4. The recorded acceleration at ground surface (Figure 5) and bottom of liquefied layer was used to evaluate shear strain and shear stresses. The degradation in stress strain

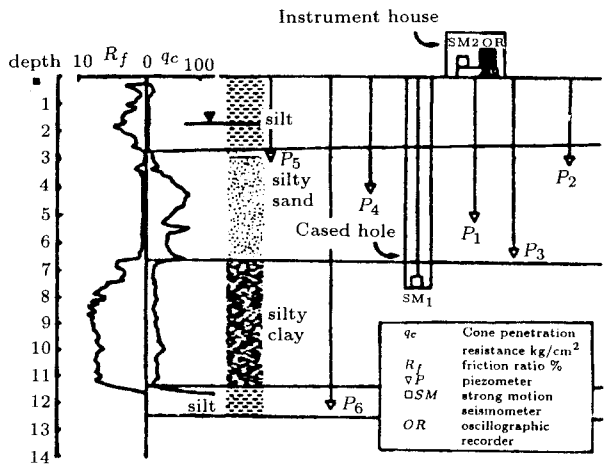

Figure 4. Cross-section and instrumentation at the Wildlife Site. Reprinted from Elgamal [3], NCEER.

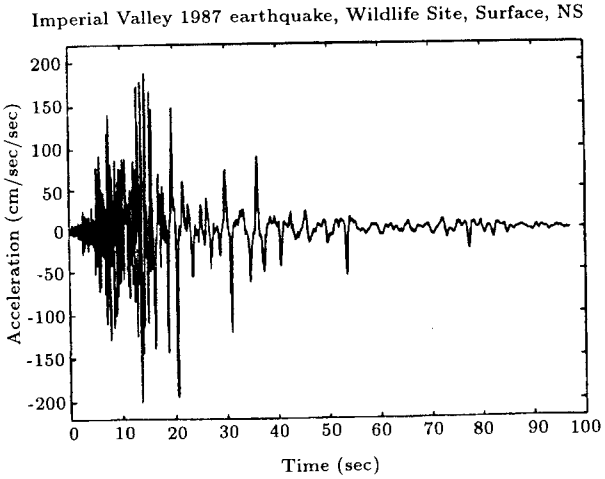

Figure 5. Recorded acceleration at the ground surface, NS Component, during the November 24, 1987 earthquake. Reprinted from Elgamal [3], NCEER.

behavior is shown in Figure 6. The actual rise of pore pressure during the earthquake of the Wildlife Site in the Imperial Valley 1987 is presented in Figure 7. These measurements during actual earthquakes are rare and contribute significantly to liquefaction behavior. It is interesting to note from these figures that spikes in earthquake record contribute to spikes in pore pressure rise, and these pore pressure rises contribute significantly to soil softening and liquefaction, starting from 14 seconds and reaching almost complete softening at 37 seconds.

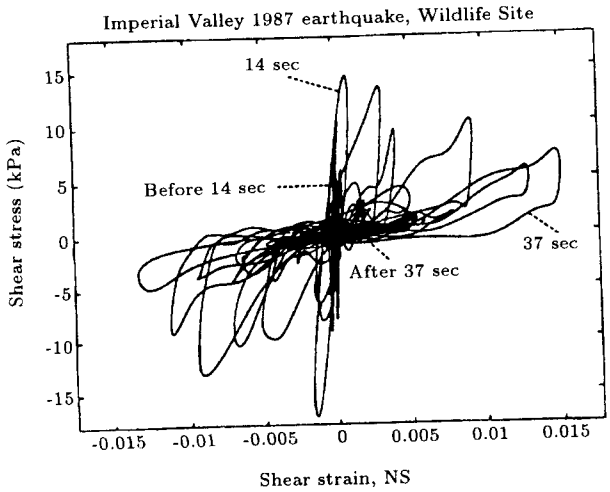

Figure 6. Average stress-strain time history during the November 24, 1987 earthquake. Reprinted from Elgamal [3], NCEER.

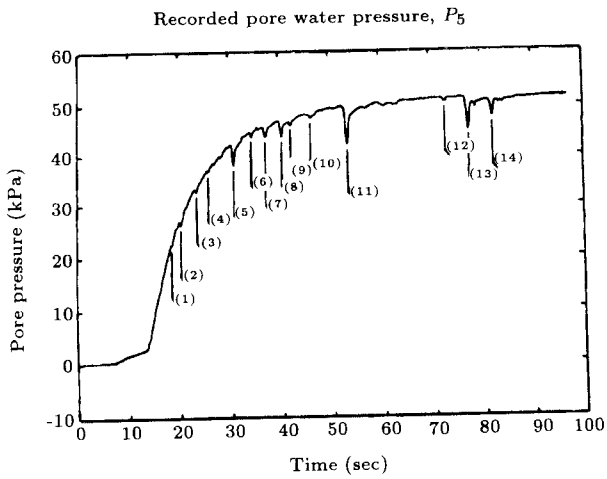

Figure 7. Pore water pressure measured by P_5, during the November 24, 1987 earthquake. Reprinted from Elgamal [3], NCEER.

Liquefaction Predictions by Field Performance

Methods of prediction of liquefaction potential are usually expressed in graphs showing cyclic stress ratio due to earthquake versus standard penetration, cone penetration or shear wave velocity. The cyclic stress ratio is expressed as:

$$\frac{\tau}{\sigma'_{vo}} = 0.65\frac{a_{max}}{g}(1 - 0.0127z)\frac{\sigma_{vo}}{\sigma'_{vo}}C \ , \qquad (1)$$

where τ is shear stress, σ'_{vo} is vertical effective stress, σ_{vo} is the total vertical stress, z is the depth in meters, a_{max} is the maximum acceleration due to earthquake and g is the acceleration of gravity. C is chosen as 0.89, 1, 1.13, 1.32 and 1.5 for earthquake magnitude M of $8^{1/2}$, $7^{1/2}$, $6^{3/4}$, 6 and $5^{1/4}$ respectively. There have been several new measurements of sites that give validity to the above evaluations. Mitchell [4] did extensive standard penetration tests, cone penetration tests and shear wave velocity measurements for the Loma Prieta earthquake 1989 and presented the results for liquefied and non liquefied sites. A sample of such testing of the profile is shown in Figure 8. It should be emphasised that field tests were run independently at the same site and no correlation formula was used. The following standardisation was used which is normal in liquefaction studies. For the standard penetration

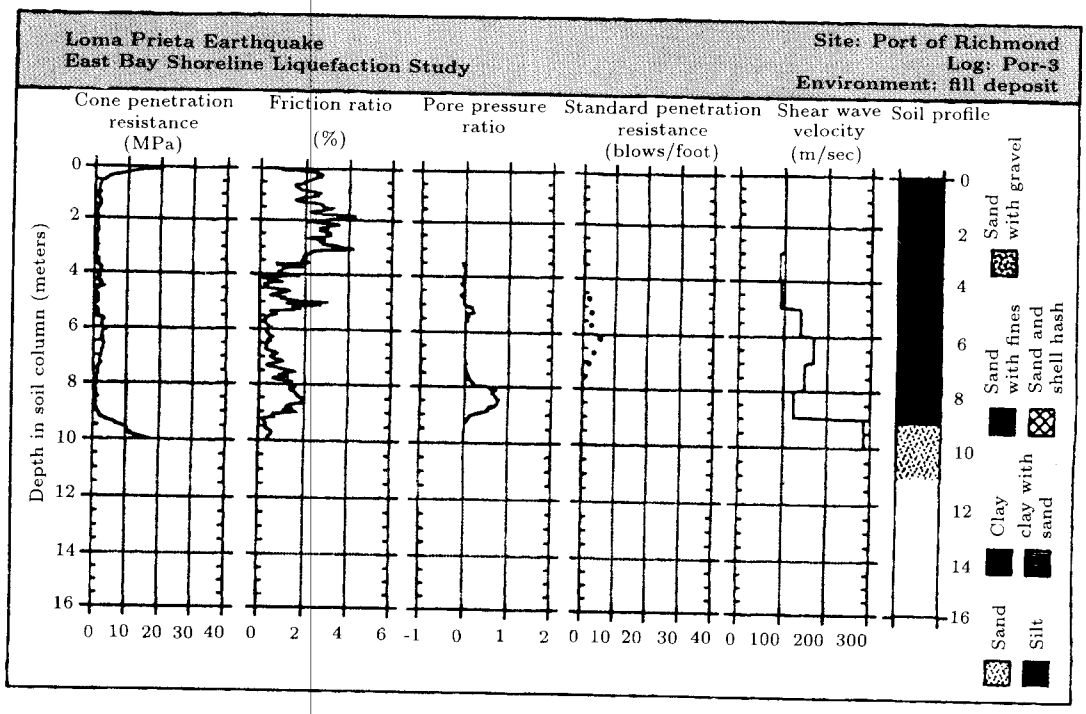

Figure 8. In-situ soil investigation log POR-3 at the Port of Richmond test site. Reprinted from Mitchell [4], NCEER.

test the following equations are used:

$$N_1 = C_n\, N\ , \tag{2}$$

$$C_n = \frac{2.2}{1.2 + \left(\frac{\sigma'_{vo}}{\sigma'_{ref}}\right)}\ , \tag{3}$$

$$(N_1)60 = N_1\left(\frac{\text{measured efficiency}}{60\%}\right)\ , \tag{4}$$

where N_1 is corrected standard penetration number, N is the measured standard penetration number, C_n is the correction coefficient, σ'_{vo} is the normal effective stress and σ'_{ref} is the atmospheric pressure. $(N_1)60$, which is the corrected number of blows per foot for 60% energy along with reference stress, is used for plotting points in the performance curve. Figures 9, 10 and 11 are estimated for the Loma Prieta earthquake for critical soil layers along the East Bay Shoreline. Figure 9 shows the performance curve for the standard penetration curve. It is clear that these new liquefaction results validate the liquefaction performance curve for standard penetration. For cone penetration tests, standardisation follows the same

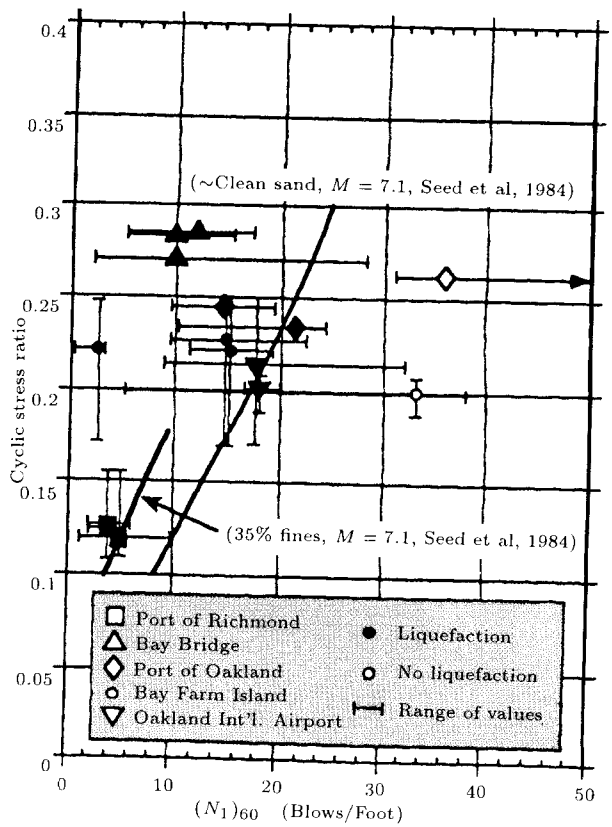

Figure 9. Standard penetration test resistance, $(N_1)_{60}$, versus cyclic stress ratio. Filled and open symbols indicate liquefaction observations. Reprinted from Mitchell [4], NCEER.

procedures as q_c of cone resistance, f_s of side resistance and U of pore pressure measured by piezocone:

$$F_r = \frac{f_S}{q_c - \sigma_{vo}} \times 100 \quad \text{friction ratio} , \tag{5}$$

$$B_q = \frac{u - u_o}{q_c - \sigma_{vo}} \quad \text{pore pressure ratio} , \tag{6}$$

$$q_{c1} = T_q \, q_c , \tag{7}$$

$$T_q = \frac{1.8}{0.8 + \frac{\sigma'_{vo}}{\sigma'_{ref}}} , \tag{8}$$

where q_{c1} is the corrected cone resistance and C_n is the correction coefficient. Figure 10 shows the results of liquefaction performance. For shear wave velocity the normalisation is expressed by the following:

$$V_{s1} = V_s \left[\frac{\sigma'_{ref}}{\sigma'_{vo}}\right]^{0.25} , \tag{9}$$

where V_s is the measured shear wave velocity and V_{s1} is the normalised shear wave velocity. The performance curve for shear wave velocity is shown in Figure 11. Mitchell, thus, presents a new curve for cyclic stress ratio versus shear wave velocity.

Validation of liquefaction potential, also presented by O'Rourke [5], for another site after Loma Prieta earthquake is shown in Figure 12. The validation leads to a strong support for the evaluation of liquefaction potential by field performance. It should be mentioned that the Japanese method calculates resistance factor against liquefaction FL, for liquefaction strength R and shear stress induced by the earthquake L from the following formula:

$$FL = \frac{R}{L} , \tag{10}$$

FL is similar to the definition of factor of safety

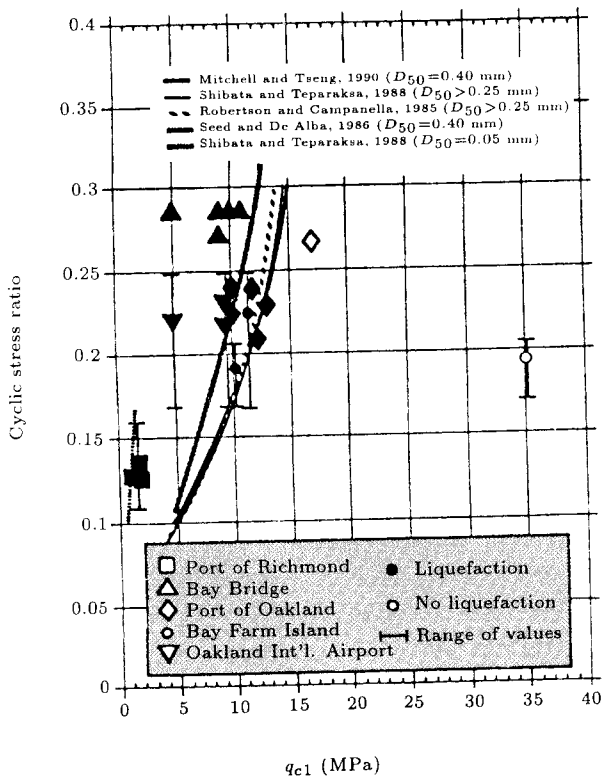

Figure 10. Cone penetration test resistance, q_{c1}, versus cyclic stress ratio. Filled and open symbols indicate liquefaction observations. Reprinted from Mitchell [4], NCEER.

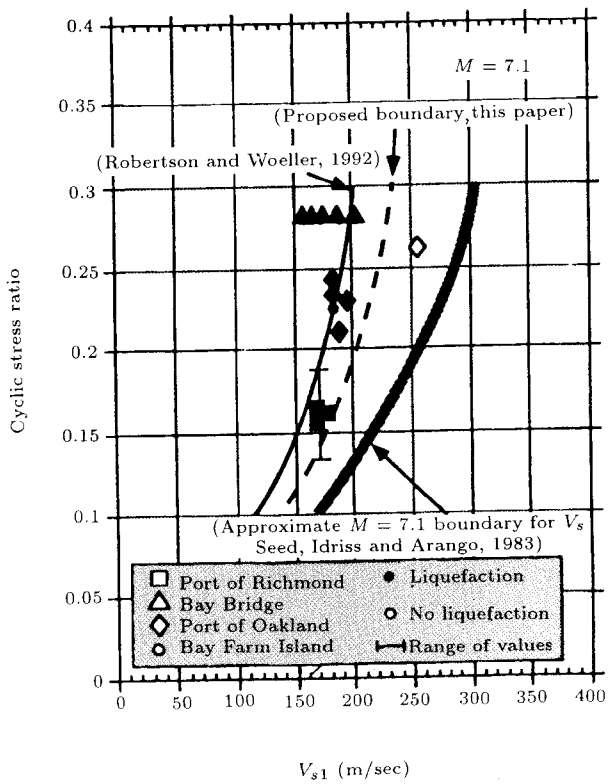

Figure 11. Overburden normalized shear wave velocity, V_{s1}, versus cyclic stress ratio. Filled and open symbols indicate liquefaction observations. Reprinted from Mitchell [4], NCEER.

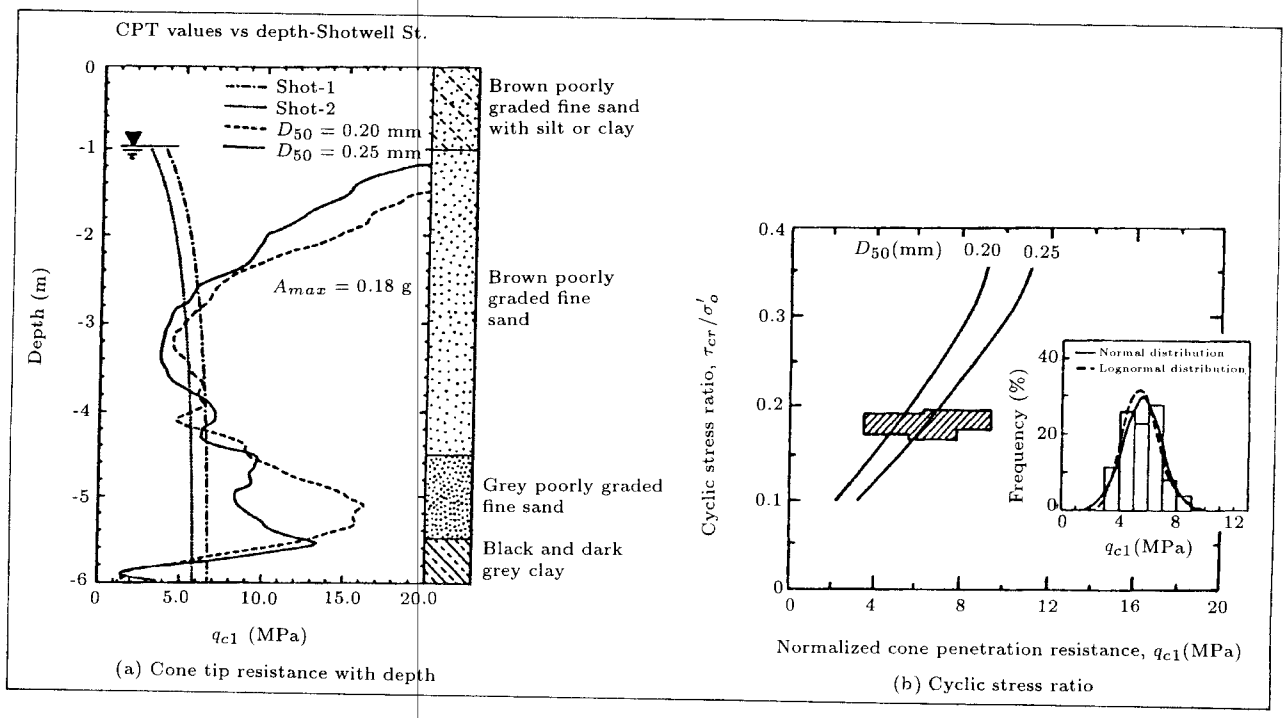

Figure 12. Cone tip resistance and cyclic stress ratio. Reprinted from O'Rourke [5], NCEER.

for liquefaction:

$$L = \frac{a_{max}}{g}(1 - 0.015z)\frac{\sigma_{vo}}{\sigma'_{vo}} , \tag{11}$$

$$R = R_1 + R_2 + R_3 . \tag{12}$$

R_1 is the evaluation of standard penetration number N,

$$R_1 = 0.0882\sqrt{\frac{N}{\sigma'_{vo} + 0.7}} , \tag{13}$$

where σ'_{vo} is expressed in kg/cm^2. R_2 is the effect of grain size:

$$R_2 = \begin{cases} 0.19 & (0.02 \text{ mm} \leq D_{50} \leq 0.05 \text{ mm}) \\ 0.225 \log_{10}(0.35/D_{50}) & (0.05 \text{ mm} < D_{50} \leq 0.60 \text{ mm}) , \\ -0.05 & (0.60 \text{ mm} < D_{50} \leq 2.00 \text{ mm}) \end{cases} \tag{14}$$

where D_{50} is 50% of the size in mm. R_3 is the effect of fine content passing through sieve 200:

$$R_3 = \begin{cases} 0.0 & (0\% \leq F_c \leq 40\%) \\ 0.004F_c - 0.16 & (40\% < F_c \leq 100\%) \end{cases} \tag{15}$$

Pattern Recognition for Liquefaction Potential

The pattern recognition method developed by Yigina and Berrill [6] has a major influence in liquefaction potential predictions. It chooses seven variables of point resistance: sleeve friction ratio, pore pressure parameter, excess pore pressure, average cyclic stress ratio, pore pressure parameter B_q and speed of the probe as points in the pattern space. The end result is the probability of pattern being in one of the three states: liquefiable soils, non-liquefiable cohesive soils and non-liquefiable cohesionless soils. Training pattern derived from field data (piezocone and CPTU data) and maximum ground accelerations from sites in New Zealand were used to design the pattern recognition system. Figure 13 shows one of their results indicating that the soil is liquefiable between depth of 2.2 to 3.2 m, 3.7 to 3.9 m and 6 to 6.5 m, where $A_{max} = 0.182g$ and CPTU = WT5012. Here the probability of soils being in liquefiable soils is greater than the probability of it belonging to either of the other two classes. The soil log is shown in

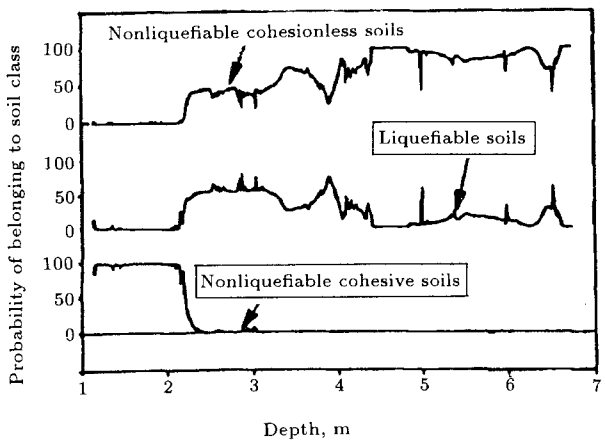

Figure 13. Liquefaction potential evaluated for soils at site A on W. Turner's farm.

Figure 14 (the results related to this figure were not included in the training or test sets).

Liquefaction Susceptibility Map

The liquefaction susceptibility map for liquefaction zoning as presented by Tinsley [7] and given in Tables 1 and 2, shows widespread utility during the Loma Prieta earthquake and the fact that the liquefaction zoning map is quite useful for large areas where actual soil measurements are not yet available.

Lateral Spread During Liquefaction

The estimated lateral spread is done by Hadata equation:

$$D = 0.75H^{0.5}\theta^{0.33} , \tag{16}$$

where D is the horizontal ground displacement in meters, H is the thickness of liquefied layer

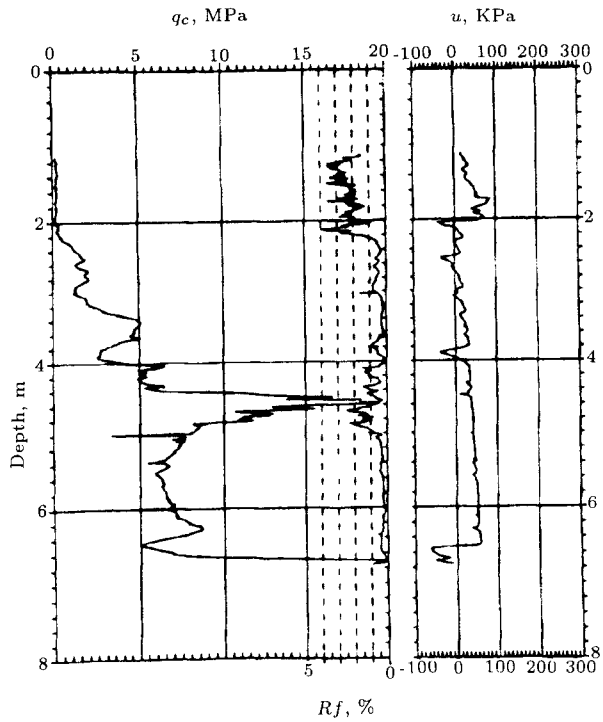

Figure 14. CPTU log from site A, which was liquefied in the 1991 Westport earthquake, on W. Turner's farm at Inangahua.

in meters and θ is the maximum ground slope in percent. Another widely used equation is:

$$\log \mathrm{LSI} = -3.49 - 1.86 \log R + 0.98M , \tag{17}$$

where LSI, the liquefaction severity index equivalent to lateral spread in inches, is evaluated. R is the distance to the epicenter in kilometers. Bartlett [8], after correlation of lateral spread, presents the following formula

Table 1. Probable susceptibility to liquefaction of cohesionless, granular, non-gravelly deposits, used to compile liquefaction susceptibility map.

Age	Depth to Water Table			
	0-10 ft	10-30 ft	30-50 ft	50+ ft
Holocene:				
Latest.....	Very High-High	Moderate	Low	Very Low
Pre-latest.....	High	Moderate	Low	Very Low
Late Pleistocene	Low	Low	Very Low	Very Low
Pre-late Pleistocene	Very Low	Very Low	Very Low	Very Low

Table 2. Description of zones of relative liquefaction susceptibility.

Very High	Very likely to liquefy in the event of even a moderate earthquake. Sediments characterized by high susceptibility to liquefaction (on the basis of engineering tests and high water table) and for which there is evidence of extensive liquefaction induced ground failure in the 1906 earthquake. Chiefly restricted to younger flood-plain deposits, but also includes some basin deposits, and estuarine, beach and some dune sands in the vicinity of the coast.
High	Likely to liquefy in the event of a nearby major earthquake. Includes sediments for which engineering tests, shallow water tables and nearby free faces indicate high susceptibility for liquefaction and resultant ground failure, but for which no historical evidence for liquefaction has been reported. Includes some basin deposits and younger flood-plain deposits, as well as most undifferentiated alluvial deposits and abandoned channel-fill deposits.
Moderate	May liquefy in the event of a nearby major earthquake. Includes sediments for which moderate susceptibilities were calculated but which lack historical evidence of liquefaction, as well as sediments with high susceptibilities but where water table is between 10 and 30 ft below the ground surface. Includes beach and older flood-plain deposits, most basin and colluvium deposits, most undifferentiated alluvial deposits and some Holocene aeolian deposits.
Low	Unlikely to liquefy, even in the event of a nearby major earthquake. Includes younger Pleistocene deposits (older dunes and landslide deposits), as well as Holocene deposits where the water table is more than 30 ft deep (for example, most of the alluvial fan deposits and some older flood-plain deposits in areas where groundwater pumping has lowered the water table).
Very Low	Very unlikely to liquefy, even in the event of a nearby major earthquake. Includes all pre-late Quaternary deposits.
Variable	Restricted to areas of artificial fill. Susceptibility to liquefaction may range from very high to low depending on the type of fill and method of emplacement. Much liquefaction-induced ground failure associated with the 1906 earthquake occurred in hydraulically emplaced fill over bay and estuarine muds.

for free face conditions:

$$\begin{aligned}\text{LOG}(D_H + 0.01) &= -16.366 + 1.178M \\ &\quad - 0.927\text{LOG}R - 0.013R + 0.657\text{LOG}W \\ &\quad + 0.348\text{LOG}T_{15} + 4.527\text{LOG}(100 - F_{15}) \\ &\quad - 0.922D50_{15} \ , \end{aligned} \tag{18}$$

and for ground slope conditions:

$$\begin{aligned}\text{LOG}(D_H + 0.01) &= -15.787 + 1.178M \\ &\quad - 0.927\text{LOG}R - 0.013R + 0.429\text{LOG}S \\ &\quad + 0.348\text{LOG}T_{15} + 4.527\text{LOG}(100 - F_{15}) \\ &\quad - 0.922D50_{15} \ , \end{aligned} \tag{19}$$

where:

M = Earthquake magnitude (moment magnitude)

R = Horizontal distance from source (km)

W = 100 (height H of free face/distance L from the face)

S = Ground slope (%)

T_{15} = Cumulative thickness of saturated granular layers with $N_1 60 \leq 15$, (m)

F_{15} = Average of fines content of saturated granular layers included in T_{15} (mm)

$D50_{15}$ = Average mean grain size in layers included in T_{15} (mm)

Lowe [9] presentation of liquefaction induced lateral spread probability matrix is shown in Table 3. MMI and corresponding probabilities of lateral spreads are defined relative to soil environments in which liquefaction is likely to occur under strong earthquake shaking. These environments include active flood plains, deltas and other areas of gently-sloping late Holocene fluvial deposits and loose sandy fill below the water table generally placed by end dumping or hydraulic fill methods. For liquefaction-susceptible environments, the water table generally should be within 3 to 5 m of the ground surface. The liquefaction failure state scale is as follows:

Light: General maximum differential movement: ≤ 1 cm; equivalent LSI < 1.

Moderate: General maximum differential movement: 1 to 10 cm; equivalent LSI: 1-5.

Heavy: General maximum differential movement: 10 to 75 cm; equivalent LSI: 5-30.

Severe: General maximum differential movement: 75 to 230 cm; equivalent LSI: 30-90.

Catastrophic: General maximum differential movement > 230 cm; equivalent LSI > 90.

The estimation of the size of lateral spread which belongs to Ariman is shown in Table 4 from Honegger [10].

Table 3. Liquefaction-induced lateral spread probability matrix.

Liquefaction Failure State	MMI VI	VII	VIII	IX	X	XI	XII
Light	75	50	20	10	0	0	0
Moderate	20	30	40	25	15	10	0
Heavy	5	20	30	40	35	25	20
Severe	0	0	10	20	35	40	30
Catastrophic	0	0	0	5	15	25	50
P_Σ	100%	100%	100%	100%	100%	100%	100%

Table 4. Estimates of lateral spread geometry based on LSI.

		Liquefaction Susceptibility Index, LSI		
		10	40	100
Spread Length, Feet	Minimum	40	85	175
	Average	95	155	275
	Maximum	650	1100	2000
Spread Width, Feet	Minimum	80	85	100
	Average	380	400	450
	Maximum	850	1150	1750

Vertical Strain Post Liquefaction

Vertical strain of liquefied soil has a major influence on damage imposed on lifelines. Due to Loma Prieta earthquake in Marina District, Pease [11] showed that the contours of repair of over 300 m of water pipes correspond closely to settlement contours from the vertical strains imposed on liquefied soil after the earthquake (Figures 15 and 16). O'Rourke while delivering the key note lecture on liquefaction

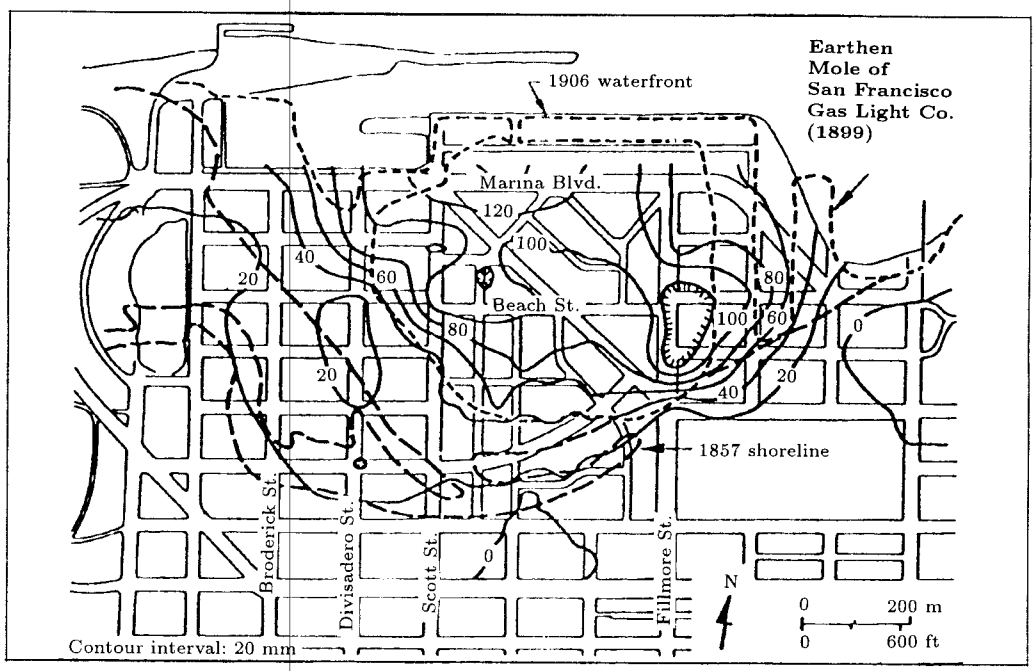

Figure 15. Settlement from post liquefaction consolidation in the Marina. Reprinted from Pease [11], NCEER.

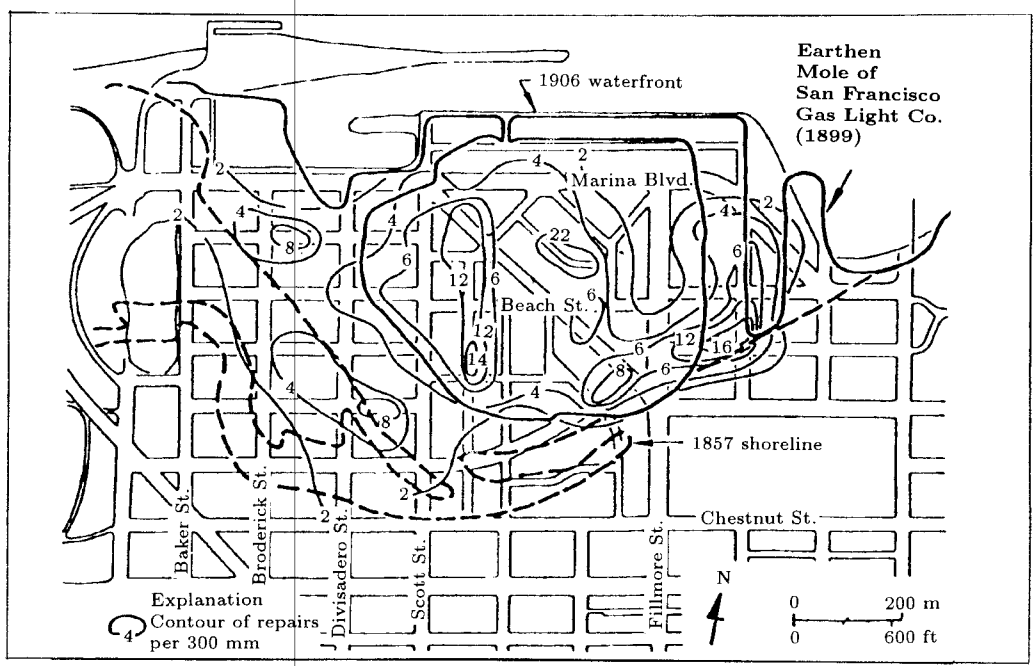

Figure 16. Contours of repair per 300 m of MWSS pipeline in the Marina. Reprinted from Pease [11], NCEER.

damage at the Third International Conference on Recent Advances in Geotechnical Earthquake Engineering and Soil Dynamics at St. Louis Missouri, 1995, indicated that the major cause for pipe damages were due to transient shears during an earthquake and not due to settlements as perceived previously. However, he demonstrated that there is a good correlation between transient shears and settlements. Thus, hisearlier conclusion still holds, although the phenomena causing the damage is transient shear, not the strains due to settlements. He proposed Table 5 for evaluation of settlement strain and used the curve of Ishihara presented in Figure 17 for post-liquefaction volumetric strain prediction.

Table 5. Observed vertical strains.

Deposit Type	Percent Liquefiable	Settlement Strain, %
Recent Natural Sand (Strawberry Island)	100	0.2
Land-Tipped Fill	100	1.5
Hydraulic Fill	55	3.7

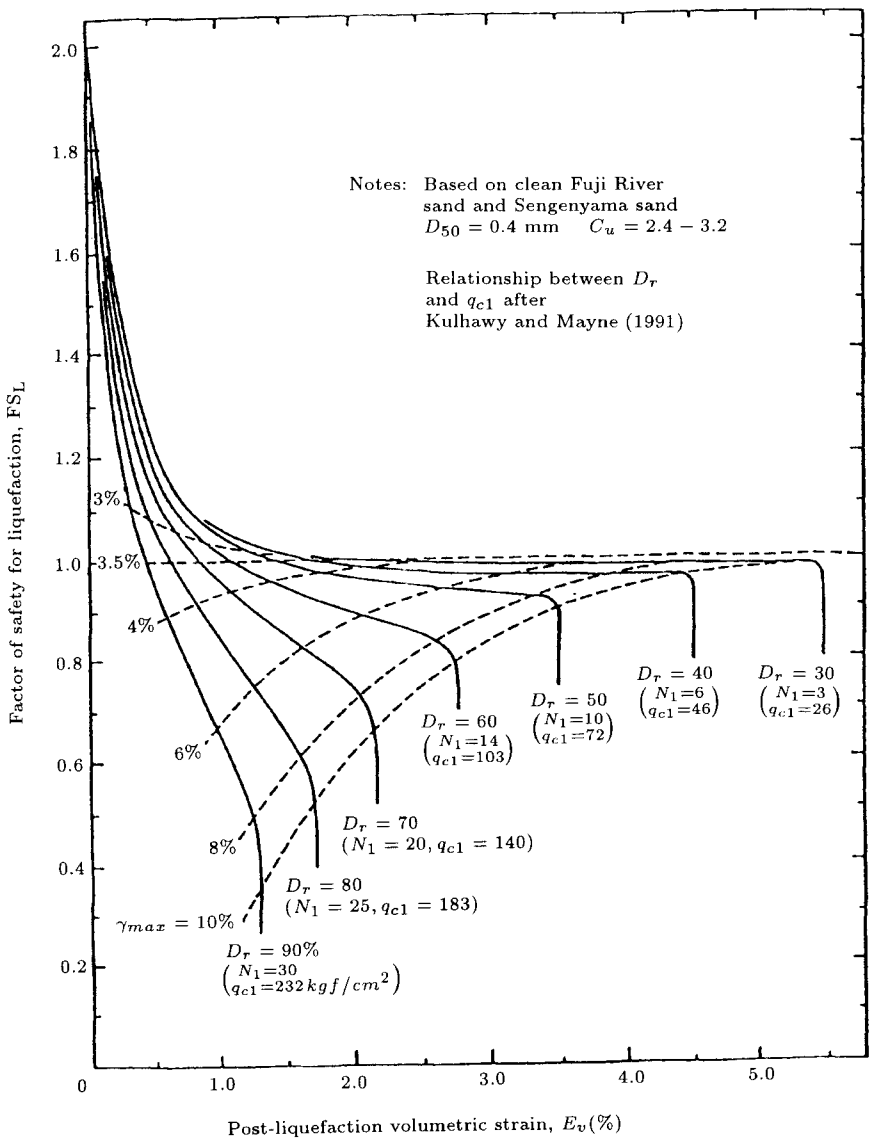

Figure 17. Relationship among volumetric strain, factor of safety for liquefaction, and in-situ density. Reprinted from Pease [11], NCEER.

Spectral Analysis of Surface Waves

The measurement of shear wave velocity by using surface method has resulted in automatic evaluation. The controlled source spectral analysis of surface waves CSSASW proposed by Satoh [12] uses a surface generator and two vibration detectors (Figure 18) by plotting coherence and phase delay between the two signals. In Figure 19, the velocity profile is calculated. Figure 20 shows good correlation of shear wave velocity prediction with other methods such as cross-hole. The evaluation of shear wave velocity is done automatically by computer. The cross-power spectrum $S_{r1,r2}(f)$ between the two signals is defined as [13]:

$$\overline{S}_{r1,r2}(f) = \frac{1}{n}\sum_{i=1}^{n}\{[R_1(f)]_i[R_2^*(f)]_i\}\ , \qquad (20)$$

where $R_1(f)$ and $R_2(f)$ correspond to Fourier transforms of time records from two receivers located a distance apart. If n records are taken, they are averaged.

The coherence function $\gamma^2(f)$ is defined as:

$$\gamma^2(f) = \frac{|S_{r1,r2}(f)|^2}{\bar{A}_{r1}(f)\cdot\bar{A}_{r2}(f)}\ , \qquad (21)$$

where $\bar{A}_{r1}(f)$ and $\bar{A}_{r2}(f)$ correspond to auto power spectra of each signal,

$$\bar{A}_r(f) = \frac{1}{n}\sum_{i+1}^{n}\{[R(f)]_i[R^*(f)]_i\}\ . \qquad (22)$$

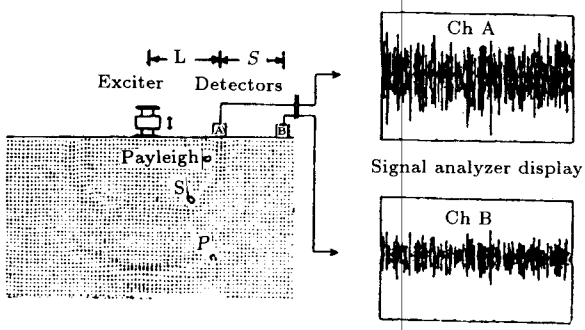

Figure 18. Random excitation as received by the detectors. Reprinted from Satoh [12], NCEER.

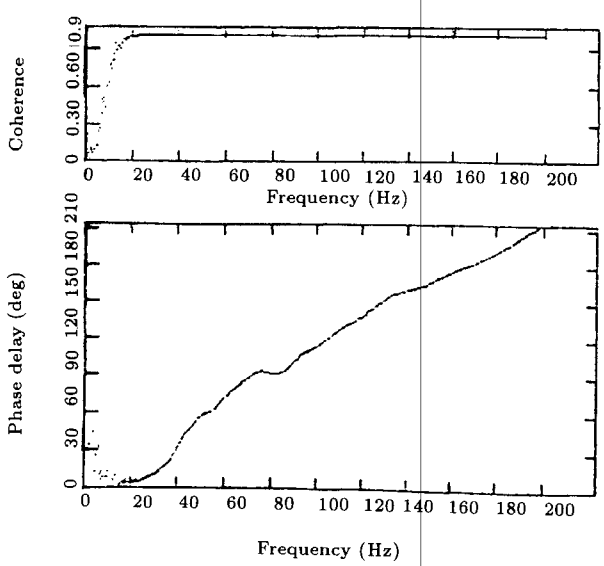

Figure 19. Coherence and phase delay functions versus frequency. Reprinted from Satoh [12], NCEER.

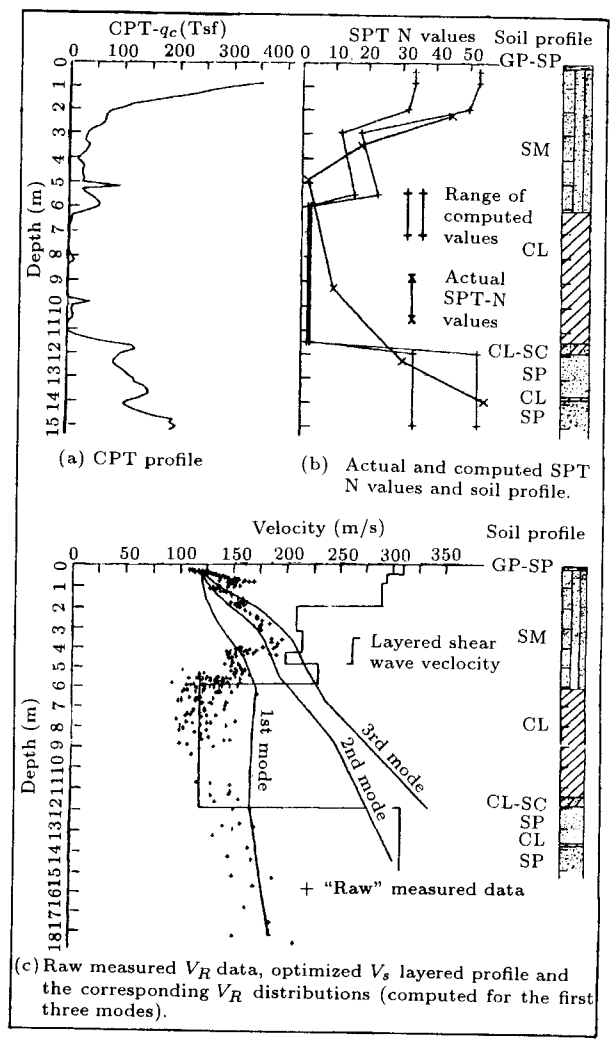

Figure 20. Typical data from the Port Site. Reprinted from Satoh [12], NCEER.

The (*) denotes the conjugate. ϕ, the phase, is calculated as follows:

$$\phi = \tan^{-1} \frac{\text{Imag}[S_{r1,r2}(d)]}{\text{Real}[S_{r1,r2,}(d)]} , \quad (23)$$

where d is the distance between probes.The travel time then can be calculated as:

$$t = \frac{\phi}{360f} , \quad (24)$$

and the phase velocity V_{ph}:

$$V_{ph} = \frac{h}{t} . \quad (25)$$

The wave length l_{ph} is:

$$l_{ph} = \frac{V_{ph}}{f} . \quad (26)$$

Thus, assuming that $l_{ph}/2$ corresponds to the property at depth, h, graph of depth versus phase velocity can be plotted.

The optimization for calculating the actual shear wave velocity depth diagram has been automatically presumed by Satoh [12] and Nazarian [13]. However, for simple cases the following simplified formula taken from Satoh can be used (see Figure 21).

If $\bar{V}_R$ is increasing with depth such as in layer 3, then:

$$V_{R3} = \frac{\bar{V}_{R3}D_3 - \bar{V}_{R2}D_2}{D_3 - D_2} , \quad (27)$$

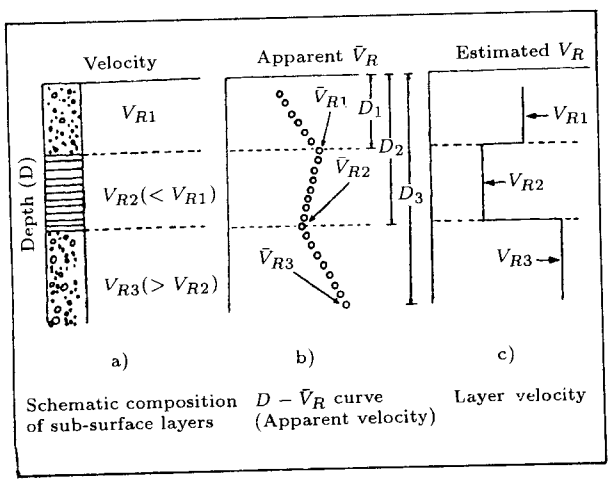

Figure 21. Simplified conversion of apparent rayleigh wave velocities. Reprinted from Satoh [12], NCEER.

and if $\bar{V}_R$ is decreasing with depth such as in layer 2, then:

$$V_{R2} = \frac{D_2 - D_1}{\frac{D_2}{\bar{V}_{R2}} - \frac{D_1}{\bar{V}_{R1}}} , \quad (28)$$

based on empirical relation:

$$V_R = 0.89V_s + 4.13 \quad \text{(m/sec)} , \quad (29)$$

then V_s is calculated.

SITE EFFECTS

The evaluation of numerous seismic records during the listed major earthquakes has made considerable progress possible in evaluation of site effects. Both linear shake 91 model and nonlinear models are used for theoretical evaluation of site effects.

Measured Site Effects

Results of measurements presented by Seed [14] for Loma Prieta earthquake are presented in Figure 22 as an example of site effects. It should become clear that many of the measured values overshoot the 1991 UBC code.

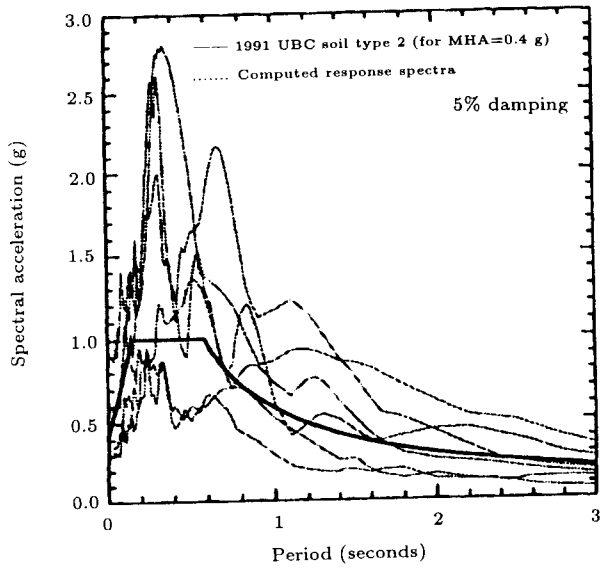

Figure 22. Computed spectral acceleration from three near-field CSMIP soil sites compared to the 1991 UBC design spectrum for soil type 2 and MHA = 0.4g. Reprinted from Seed [14], Earthquake Engineering Recearch Center (EERC).

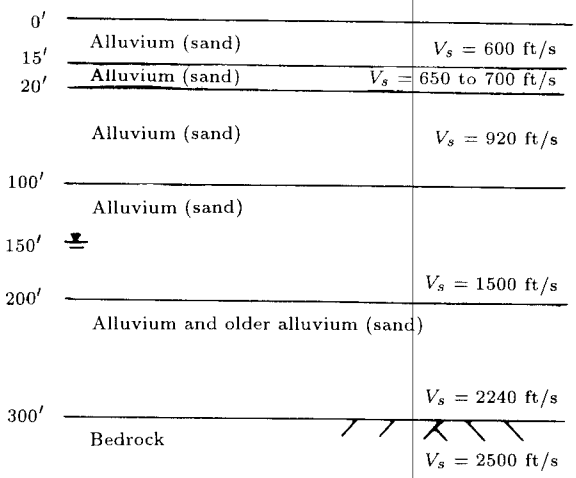

Figure 23a. Soil profile for the Sylmar-County Hospital parking lot site (Olive View Hospital). Reprinted from Seed [14], EERC.

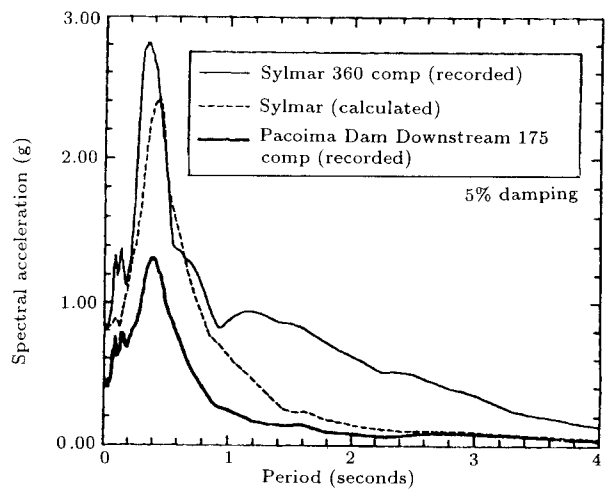

Figure 23b. Comparison of acceleration response spectra for the recorded and calculated motions at the Sylmar-County Hospital parking lot site and for the input motion at Pacoima Dam Downstream. Reprinted from Seed [14], EERC.

Calculation of Site Effects

The use of program Shake 91 and similar procedures for predicting the site effects has been carried out by Seed [14] for the Loma Prieta earthquake (Figure 23); analogous calculations are done for the Northridge 1994 earthquake by Seed [15]. The site profile and acceleration measurements at bottom and top of the layers are shown in Figure 24 and the

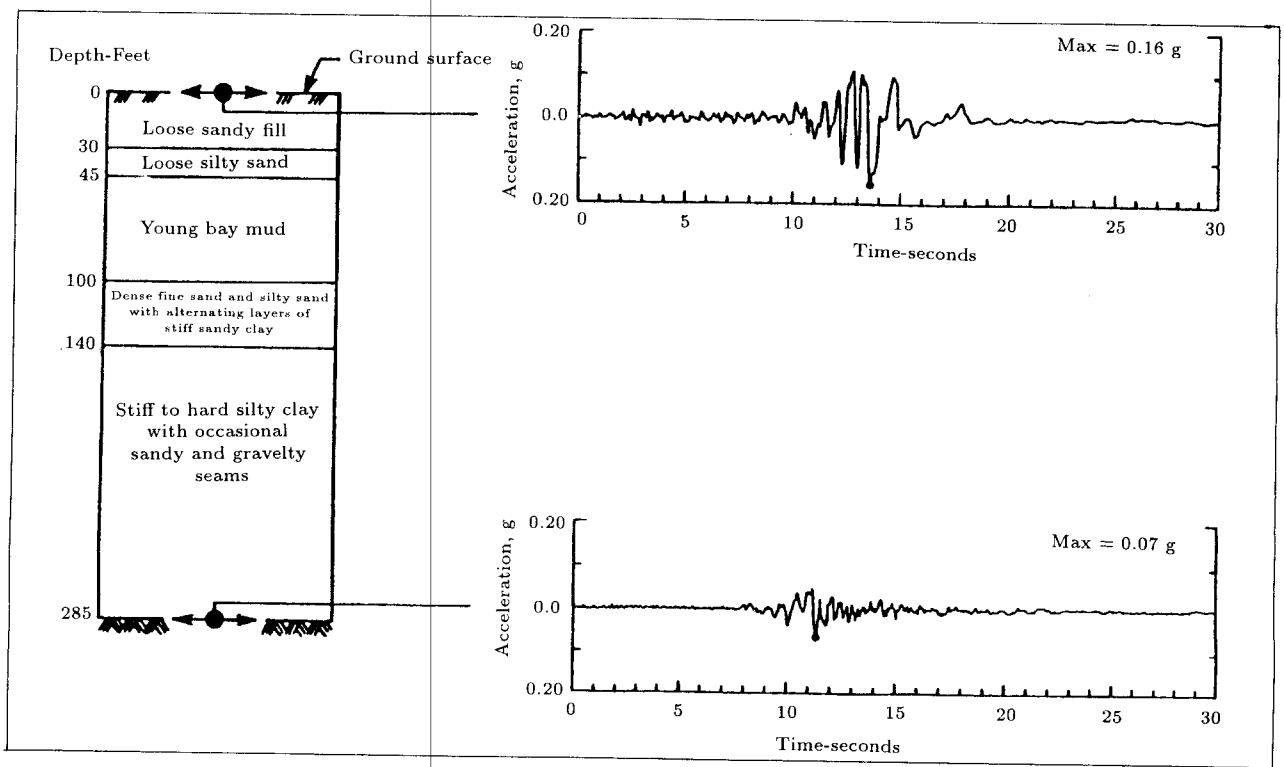

Figure 24. Schematic soil profile and site response at the Treasure Island Fire Station. Reprinted from Seed [15], EERC.

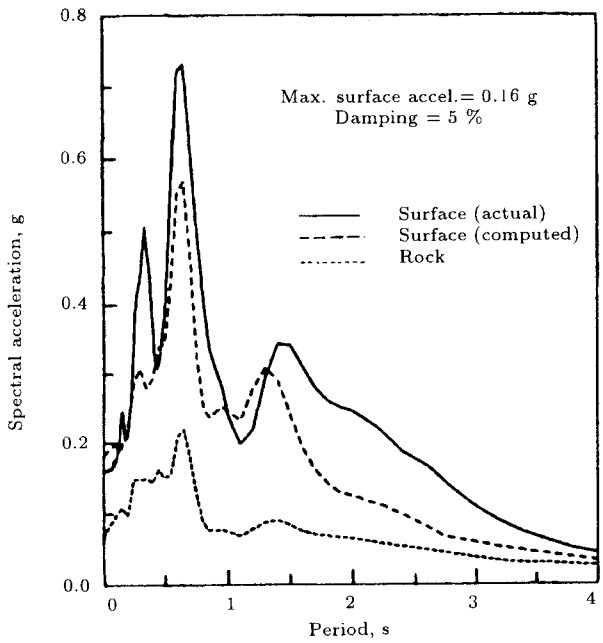

Figure 25. Comparison between calculated and recorded response spectra for Treasure Island Fire Station (90 degree comp.) Reprinted from Seed [15], EERC.

calculated response spectrum in Figure 25. It is clear from both calculated response spectra that the calculations are in good agreement up to frequency of 1-1.5, but the calculations grossly underestimate the response for larger frequencies.

Thus, spectra as presented above and similar records could have an important influence in revision of the earthquake code.

THEORETICAL DEVELOPMENTS

Theoretical developments in evaluating the earthquake and dynamic effects have progressed considerably. Because of space limitation a full review of these developments can not be given, but as an example, the theoretical development, predicted by the above mentioned evaluation, of zero extension line development at Shiraz University in Iran and at the University of Canterbury in New Zealand are summarized here.

Dynamic Active Earth Pressure

The dynamic active earth pressure as predicted by zero extension line theory is presented by Anvar [16]. Figure 26 displays the dynamic active earth pressure coefficient and the static active earth pressure coefficient. In these figures, φ is the friction angle of the soil and δ_w is the wall friction angle. The wall roughness can also be presented by C_r, being zero for a smooth wall and one for a completely rough wall. Also, h is the depth and ρ is the soil density. It is shown that:

$$p = k_{as}\rho g h + k_{ad}\rho k_h h \qquad (30)$$

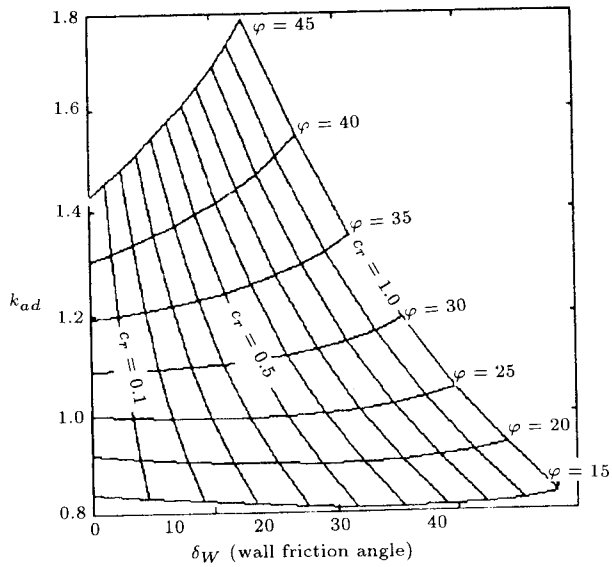

Figure 26a. Dynamic active earth pressure coefficient.

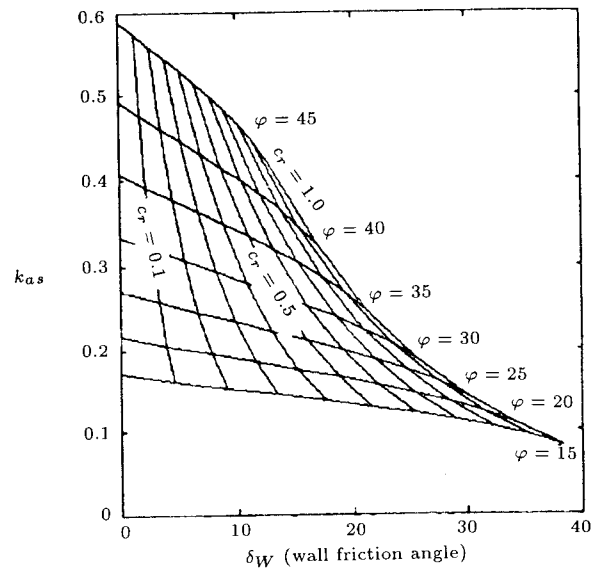

Figure 26b. Static active earth pressure coefficient.

where K_{as} is the active static earth pressure coefficient, k_{ad} is the dynamic active earth pressure coefficient, k_h is the fraction of horizontal gravity acceleration and h is the depth. The results are also presented in a revision to the Building Code of Iran Seismic Code proposed in 1993 by Behpoor [17].

Seismic Beam Capacity Factors

The zero extension line research has been applied to bearing capacity calculations during seismic loading. The results for clay soils are presented by Ghahramani [18] in Figure 27 for $k_h = 0.3$.

Considerable reduction in N_c is obvious. The evaluation formula for clay soils is:

$$p = C\ N_c + q\ N_q - \frac{1}{2}\gamma\ b\ k_h\ N_\gamma\ , \qquad (31)$$

where C is the cohesion, q is surcharge, p is bearing capacity, b is the width of the footing, N_γ is the inertial bearing exponent factor, N_c the cohesion bearing capacity factor and N_q is the surcharge bearing capacity factor. The formula presented below closely approximates the theoretical curves for up to $k_h = 0.3$:

$$N_c = (\pi + 2)(1 - 1.1k_h - 0.59k_h^2)\ , \qquad (32)$$

$$N_q = 1 - 2.5k_h\ , \qquad (33)$$

$$N_\gamma = 3.58(1 - 2.35k_h)\ . \qquad (34)$$

The above equations demonstrate that during the seismic conditions the bearing capacity of clay soils is highly reduced.

The results for sandy soils are presented by Ghahramani [19] in Figure 28, where N_q is a function of ϕ friction angle and k_h the horizontal acceleration ratio. Results for N_γ are presented in Figure 29 and ratio of N_γ for seismic conditions to N_γ for static conditions are shown in Figure 30. The formula for calculation of bearing capacity of sandy soils is:

$$p = C\ N_c + q\ N_q + \frac{1}{2}\gamma\ b\ N_\gamma\ , \qquad (35)$$

and:

$$N_c = \cot\phi(N_q - 1)\ . \qquad (36)$$

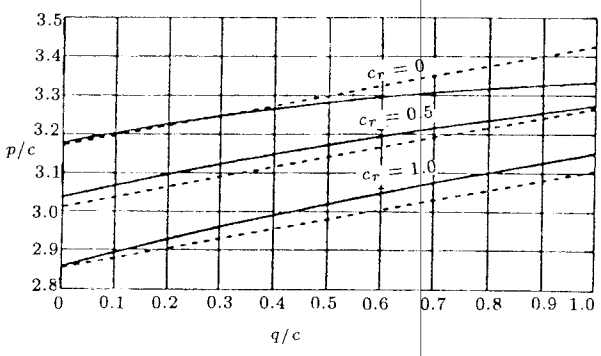

Figure 27. Bearing capacity for $k_h = 0.3$.

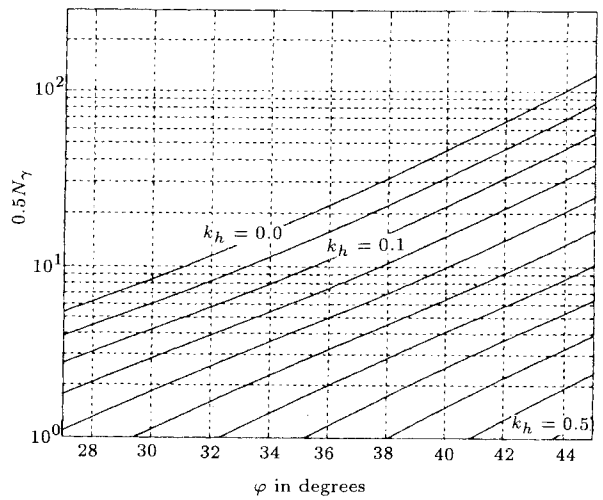

Figure 28. Bearing capacity factor 0.5 N_γ [19].

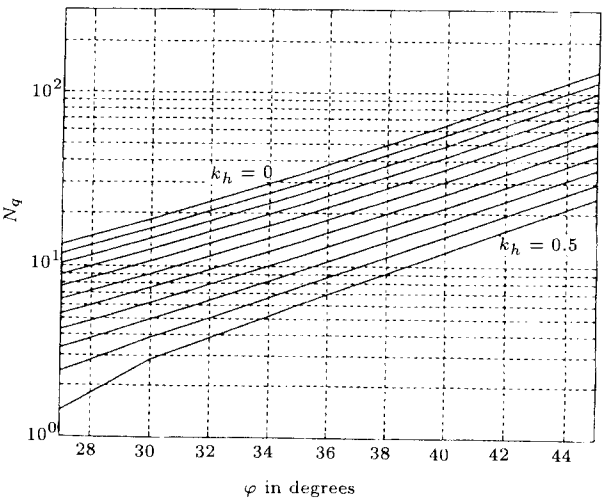

Figure 29. Bearing capacity factor N_q for $c/q = 0$ [19].

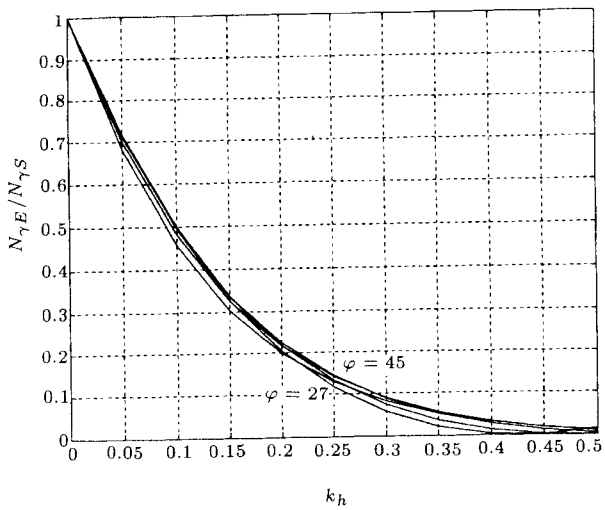

Figure 30. Seismic to static bearing capacity ratios [19].

The reduction of N_c, N_γ and N_q for seismic conditions of high k_h horizontal fraction and of peak ground acceleration imply that many bearing capacity failures can happen even when liquefaction is not triggered at the site.

CONCLUSION

The developments in geotechnique for earthquake engineering lead to better understanding in the following:

1. Liquefaction area involving:
   a. Epicentral distance predictions,
   b. Measurement of actual liquefaction during an earthquake,
   c. Field performance by standard penetration, cone penetration and shear wave velocity,
   d. Pattern recognition,
   e. Liquefaction susceptibility map,
   f. Lateral spread during earthquake,
   g. Vertical strain post liquefaction,
   h. Spectral analysis of surface waves.
2. Site effects including:
   a. Measurement,
   b. Calculation methods.
3. Theoretical developments related to estimation of:
   a. Dynamic earth pressure,
   b. Seismic bearing capacity factors.

These improvements make the prediction of earthquake geotechnical effects and performance more rational. And if it is used effectively, it can bring about major contributions in code revision, earthquake mitigation effects and long term reduction in loss of life, property and lifeline facilities.

ACKNOWLEDGEMENT

The author gratefully acknowledges the discussions with Dr. J.B. Berrill, Reader in the Civil Engineering Department, University of Canterbury and the support of Shiraz University and the University of Canterbury during his sabbatical leave. Thanks and appreciation are also expressed to the International Institute for Seismology and Earthquake Engineering for supporting partially the author's trip to Iran. The support of the National Iranian Gas Company and Moavenat Tarh va Barnameh of Bonyad is gratefully acknowledged. The author also fully acknowledges the support of Ministery of Power of Islamic Republic of Iran for attending the Third International Conference on Recent Advances in Geotechnical Earthquake Engineering and Soil Dynamics in Missouri. Special thanks are expressed to Minster of Power of Islamic Republic of Iran, engineer Zanganeh for encouraging and supporting the author during the last eight years in geotechnical engineering research.

This paper was presented at the Second International Conference on Seismology and Earthquake Engineering, May 15-17, 1995, Tehran, I.R. Iran.

REFERENCES

1. Yoshida, N., Watanabe, H., Yasuda, S. and Mora, S.C. "Liquefaction-induced ground failure and related damage to structures during 1991 Telire-Limon, Costa Rica earthquake", *Proc. Fourth Japan-USA Workshop on Earthquake Resistant*

Design of Lifeline Facilities and Countermeasures for Soil-Liquefaction, National Center for Earthquake Engineering Research, NCEER-92-0019, pp 37-52 (1992).

2. Wakamatsu, K., *Liquefaction History*, 416-1990, Japan, *Proc. Fourth Japan-USA Workshop on Earthquake Resistant Design of Lifeline Facilities and Countermeasures for Soil-Liquefaction*, National Center for Earthquake Engineering Research, NCEER-90-0019, pp 97-114 (1992).

3. Elgamal, A.W., Zeghal, M. "Analysis of Wildlife Site liquefaction during 1987 Superstition Hills earthquake", *Proc. Fourth Japan-USA Workshop on Earthquake Resistant Design of Lifeline Facilities and Countermeasures for Soil-Liquefaction*, National Center for Earthquake Engineering Research, NCEER-90-0019, pp 87-96 (1992).

4. Mitchell, J.K., Kayen, R.E., Seed, R.B., Lodge, A., Nishio, S. and Coutinho, R. "Evaluation of SPT-CPT and shear wave based methods for liquefaction potential assessment using Loma Prieta data", *Proc. Fourth Japan-USA Workshop on Earthquake Resistant Design of Lifeline Facilities and Countermeasures for Soil-Liquefaction*, National Center for Earthquake Engineering Research, NCEER-92-0019, pp 177-204 (1992).

5. O'Rourke, T.D., Meyersohu, W.D., Stewart, H.E., Pease, J.W. and Hiyajima, M. "Site response and liquefaction in San Francisco during the Loma Prieta earthquake", *Proc. Fourth Japan-USA Workshop on Earthquake Resistant Design of Lifeline Facilities and Countermeasures for Soil-Liquefaction*, National Center for Earthquake Engineering Research, NCEER-92-19, pp 53-70 (1992).

6. Yigina, D. and Berrill, J.B. "A pattern recognition approach to evaluation of soil liquefaction potential using Piezocone data", *J. Soil Dyn. and Earthquake Engng.*, **12**, pp 91-101 (1993).

7. Tinsley, J.C. and Dupte, W.R. "Liquefaction hazard mapping depositional forces and lateral spread ground failure in the Monterey Bay area, Central California during the 10/A189 Loma Prieta earthquake", *Proc. Fourth Japan-USA Workshop on Earthquake Resistant Design of Lifeline Facilities and Countermeasures for Soil-Liquefaction*, National Center for Earthquake Engineering Research, NCEER-92-19, pp 71-85 (1992).

8. Bartlett, S.F. and Youd, T.L. "Empirical prediction of lateral displacement", *Proc. Fourth Japan-USA Workshop on Earthquake Resistant Design of Lifeline Facilities and Countermeasures for Soil-Liquefaction*, National Center for Earthquake Engineering Research, NCEER-92-19, pp 351-365 (1992).

9. Lowe, A., Bivins, W. and O'Rourke, T.D. "A new method to estimate earthquake liquefaction damage to buried lifelines", *Proc. Fourth Japan-USA Workshop on Earthquake Resistant Design of Lifeline Facilities and Countermeasures for Soil-Liquefaction*, National Center for Earthquake Engineering Research, NCEER-92-19, pp 439-451 (1992).

10. Honegger, D.G. "Research needs related to detailed evaluation of pipeline response to large ground deformations", *Proc. Fourth Japan-USA Workshop on Earthquake Resistant Design of Lifeline Facilities and Countermeasures for Soil-Liquefaction*, National Center for Earthquake Engineering Research, NCEER-92-19, pp 525-540 (1992).

11. Pease, J.W., O'Rourke, T.D. and Stewart, H.E. "Post-liquefaction and lifeline damage in the Marina District after the 1989 Loma Prieta earthquake", *Proc. Fourth Japan-USA Workshop on Earthquake Resistant Design of Lifeline Fa-*

cilities and Countermeasures for Soil-Liquefaction, National Center for Earthquake Engineering Research, NCEER-92-19, pp 395-411 (1992).

12. Satoh, T., Poran, C.J. and Rodrigus, J.A. "Non-intrusive surface wave measurements for shear wave velocity profiling of liquefaction sites", *Proc. Fourth Japan-USA Workshop on Earthquake Resistant Design of Lifeline Facilities and Countermeasures for Soil-Liquefaction*, National Center for Earthquake Engineering Research, NCEER-92-19, pp 655-667 (1992).

13. Nazarian, S. and Desai, M.R. "Automated surface wave method field testing", *J. of Geotechnical Engng. Div., ASCE*, **119** (7), pp 1094-1111 (1993).

14. Seed et al. "Preliminary report on the principal geotechnical aspects of the October 17, 1989 Loma Prieta earthquake", UCB/EERC-90/05 (1990).

15. Seed et al. "Preliminary report on the principai geotechnical aspects of the January, 17, 1994, Northridge earthquake", UCB/EERC-94/08 (1994).

16. Anvar, S.A. and Ghahramani, A. "Dynamic active earth pressure against retaining walls", *Proc. Third International Conference on Recent Advances in Geotechnical Earthquake Engineering and Soil Dynamics*, St. Louis, MO, USA pp 343-346 (1995).

17. Behpoor, L.A. and Ghahramani, A. "Recommendations for evaluation of dynamic earth pressure on retaining walls for Iranian earthquake code", *Proc. Second International Seminar on Soil Mechanics and Foundation Engineering of Iran*, Tehran, Iran (1993).

18. Ghahramani, A. and Berrill, J.B. "Seismic bearing capacity factors for clay soils by zero extension line method", *Proc. Annual Conference, The New Zealand National Society for Earthquake Engineering*, Rotorua, NZ (1995).

19. Ghahramani, A. and Berrill, J.B. "Capacity factors by zero extension line method", *Proc. Pacific Conference on Earthquake Engineering*, Melbourne, Australia, submitted for publication (1995).